Science Advances
AAAS

advances.sciencemag.org/cgi/content/full/6/22/eaaz6153/DC1

Supplementary Materials for

Chemotaxis strategies of bacteria with multiple run modes

Zahra Alirezaeizanjani, Robert Großmann, Veronika Pfeifer, Marius Hintsche, Carsten Beta*

*Corresponding author. Email: beta@uni-potsdam.de

Published 27 May 2020, *Sci. Adv.* **6**, eaaz6153 (2020)
DOI: 10.1126/sciadv.aaz6153

The PDF file includes:

Other Supplementary Material for this manuscript includes the following:

(available at advances.sciencemag.org/cgi/content/full/6/22/eaaz6153/DC1)

Supplementary materials

S1 Bacterial sample preparation and image processing

Bacterial sample preparation and chemotaxis assay The fluorescent labeling of flagella of *Pseudomonas putida* KT2440 $\mathrm{FliC_{S267C}}$ followed the protocol of Ref. (*7*). Briefly, $50\,\mathrm{mL}$ of the overnight cell suspension were washed once to remove the growth medium by centrifugation ($4000\,\mathrm{rpm}$, $4\,\mathrm{min}$, room temperature), followed by gentle resuspension of the pellet in $1\,\mathrm{mL}$ of MB+ ($11.2\,\mathrm{g\,L^{-1}}$ K_2HPO_4, $4.8\,\mathrm{g\,L^{-1}}$ KH_2PO_4, $3.93\,\mathrm{g\,L^{-1}}$ NaCl, $0.029\,\mathrm{g\,L^{-1}}$ EDTA and $0.5\,\mathrm{g\,L^{-1}}$ glucose; pH 7.0). The flagellar filaments were then labeled with $50\,\mu\mathrm{L}$ Alexa Fluor 488 C5-maleimide dye (Life technologies) stock solution ($1\,\mathrm{mL}$ dye, $1\,\mathrm{mL}$ DMSO (Prolabo)) on a rocker shaker at $40\,\mathrm{rpm}$ for about $30\,\mathrm{min}$. Fluorescently stained bacteria were washed ($2500\,\mathrm{rpm}$, $1.5\,\mathrm{min}$, room temperature) with $1\,\mathrm{mL}$ of MB+ to remove free fluorescent dye. Afterwards, the cell suspension was divided into two parts. One was centrifuged and resuspended in MB+ medium (chemoattractant-free cell suspension); the other was resuspended in MB+ supplemented with the chemoattractant (casamino acids, Amresco) at a concentration of $7\,\%$ (wt/vol) to prepare the chemoattractant-containing cell suspension. In both cases, the $\mathrm{OD_{600}}$ of the cell suspensions was 0.02 before filling them into chemotaxis chambers shown in Fig. S1A.

A μ-Slide Chemotaxis 3D chamber (ibidi) was utilized to create a stable linear gradient of chemoattractant (*35*). Each chemotaxis unit has two large reservoirs and one central channel (observation area). The chemoattractant gradient is produced by diffusion across the central channel. For the chemotaxis assay, the reservoir on the right hand side was filled with the chemoattractant-containing cell suspension and the reservoir on the left was filled with MB+ chemoattractant-free cell suspension. In this way, the emergence of spurious drifts due to an inhomogeneous initial distribution of bacteria was excluded. The field of view was placed in the center of the gradient region, $30\,\mu\mathrm{m}$ above the bottom of the chamber (Fig. S1A); the to-

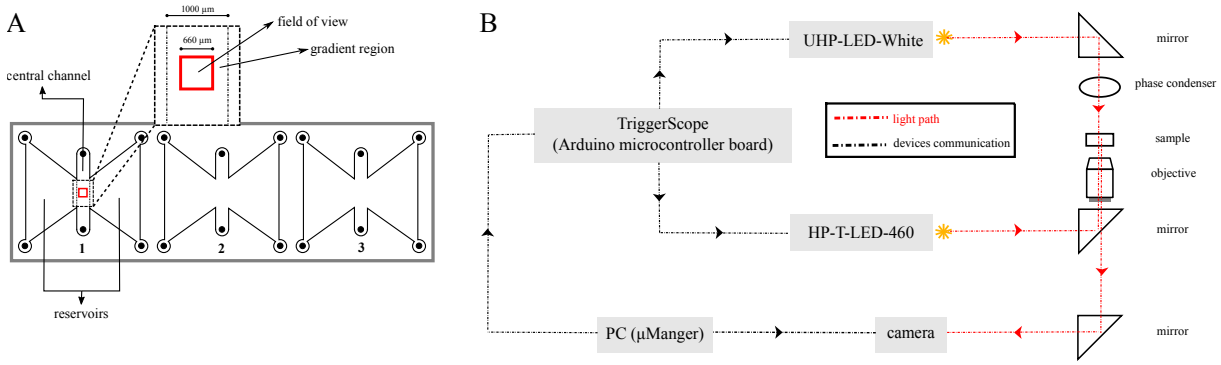

Figure S1: Schematic illustration of the chemotaxis chamber as well as the experimental setup, including the device communication. (A) Sketch of the ibidi-device containing three chemotaxis chambers. Each chamber consists of two large reservoirs connected to a central channel. In order to avoid drift as a consequence of an asymmetric initial distribution of bacteria resulting in cell migration from high to low density areas, both, right and left reservoirs were filled with bacterial suspension. In the chemotaxis assay, the right reservoir of the first chamber additionally contained the chemoattractant (casamino acids). The second chamber was used for the control experiment without a chemical gradient. Bacteria were imaged in the central area marked in red. (B) Scheme of the microscope optical path and devices communication.

tal height of the observation area was $70\,\mu\mathrm{m}$. For the bulk assay, both reservoirs carried the chemoattractant-free cell suspension in order to ensure a homogeneous environment (control experiment).

Cell imaging and tracking The image sequences were processed with an in-house, automated Matlab program based on the Image Processing Toolbox (version R2015a, The MathWorks, USA). A pixel-wise time average projection of the image stack was calculated and subtracted from each frame to remove non-motile objects and shading effects. The built-in Matlab function *imerode* was then applied for morphological erosion (with a disk of radius $0.6\,\mu\mathrm{m}$) to reduce the background noise. The cells were detected by a maximum entropy thresholding algorithm (*36*). We took the median of all threshold values calculated for individual images of the stack as threshold. In order to eliminate any noise caused by segmentation, the binary images were processed with the morphological operations *imopen* and *imclose* (with a disk of

radius $0.3\,\mu\mathrm{m}$). After that, the function *bwconncomp*, and *regionprops* were applied to cluster the pixels belonging to the putative cells and determine their sizes and centroids. The objects with an area of $1 - 15.6\,\mu\mathrm{m}^2$ were taken as single bacterial cells. Finally, by employing the tracking algorithm by Crocker and Grier (*37*), the trajectories were obtained.

S2 Exemplary trajectories

In the Figs. S2-S7, typical trajectories are exemplarily shown along with the characteristic time series of speed and rotational velocity, with a particular focus on transitions from one swim mode into another.

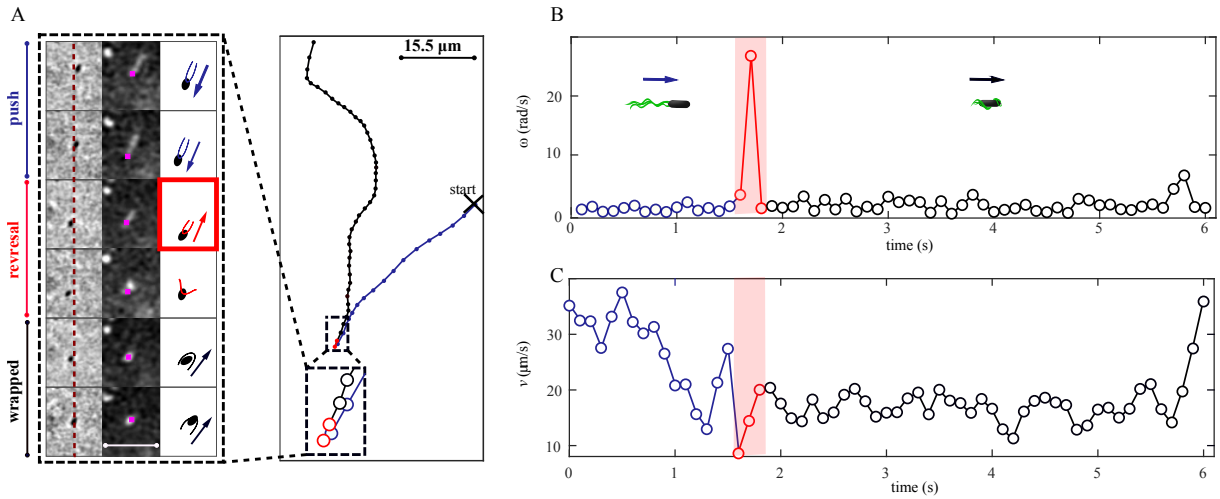

Figure S2: Cell trajectory containing a reversal as a result of a push-wrap transition. (A) The panel on the right shows the tracked cell positions. The cell swam in the push mode and, after a reversal, the flagellar bundle changed to the wrapped mode. The overlapping forward and backward parts of the trajectory close to the reversal event may be the result of a short intermediate pull phase, see the rectangular inset. The panel on the left displays the raw image series of the corresponding data points together with the schematic representations of the swim mode. The first and second columns show the phase-contrast images of the cell body and the fluorescence images of the flagellar bundle configuration (captured $0.05\,\mathrm{s}$ after the phase-contrast image), respectively. The center of mass obtained by linear interpolation between adjacent phase-contrast is marked by a pink rectangle. The dashed red line provides a guide to the eye for cell position. The flagellar bundle highlighted by a red rectangle is tightly bound and long, and may thus be the sign of a short intermediate pull mode with duration $< 0.05\,\mathrm{ms}$ (cf. Movie S2). The scale bars are $15.5\,\mu\mathrm{m}$. (B) Time series of the absolute value of the rotational velocity ω and (C) swimming speed v. The automatized event detection method identified the reversal based on the peak value of the rotational velocity ω time series at time $1.7\,\mathrm{s}$. The colour scheme is the same as Fig. 1 of the main text (here and in figures S3-S6).

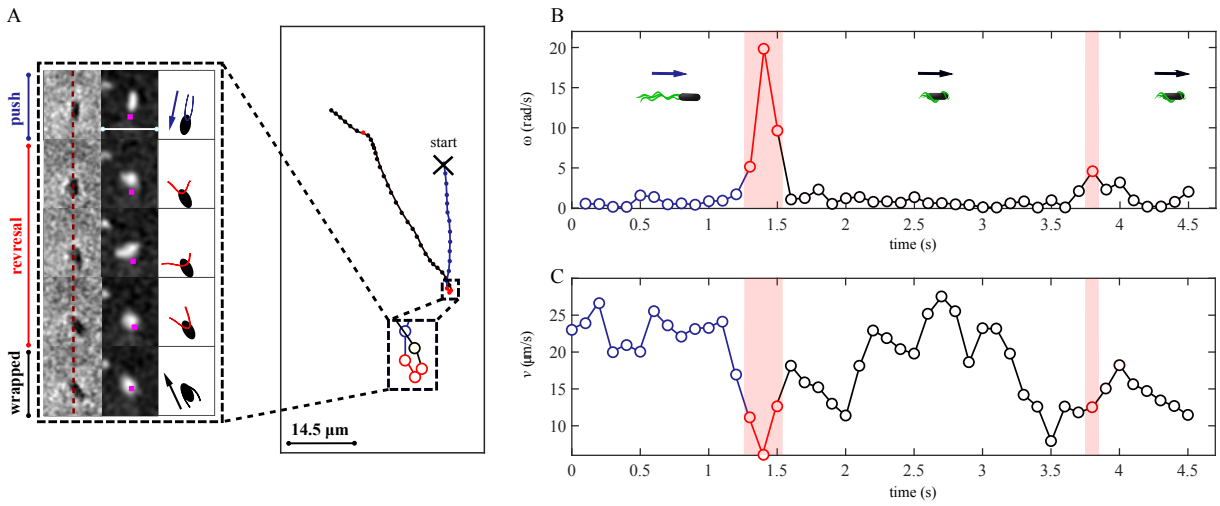

Figure S3: Push-wrap transition with a reversal of the direction of motion. (A) The trajectory contains two runs in different modes and two events. The rectangular inset shows the selected data points including the reversal event. The corresponding raw image data in the left panel shows the bundle transition from push to wrap. Initially, the bacterium swam in the push mode. After the short reversal episode, the bundle wrapped around the cell body. During the reversal, the cell body relocated forward while the bundle deformed simultaneously. This type of trajectories are an indication for direct push to wrap transitions without any intermediate phase (see also Movie S3). (B) The time series of the absolute value of the rotational velocity ω shows two peaks, one at time $1.4\,\mathrm{s}$ and the other at time $3.8\,\mathrm{s}$. (C) Speed v graph displays a deceleration during the reversal.

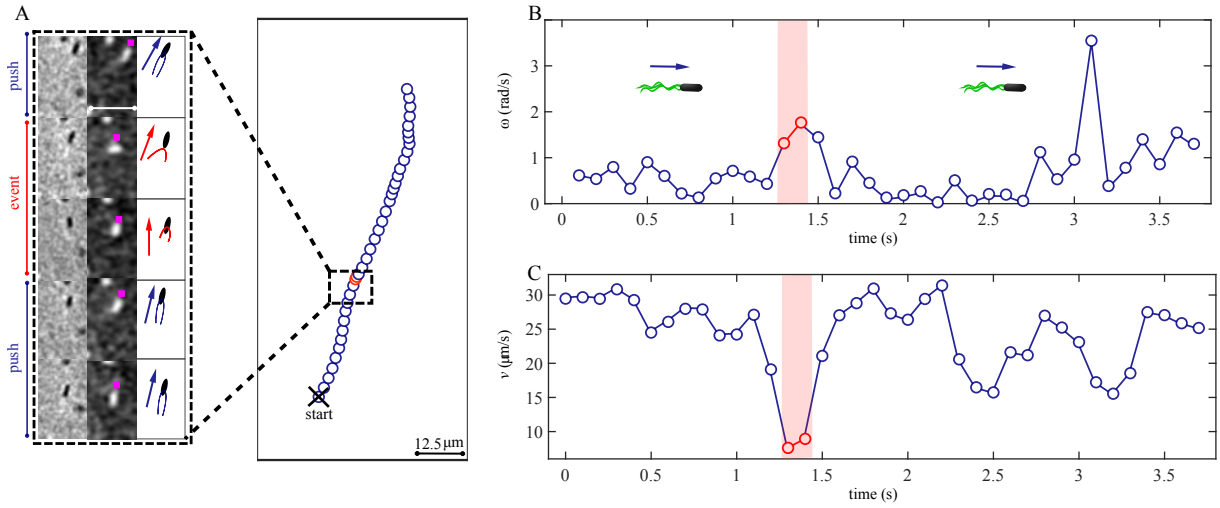

Figure S4: Relatively straight track of a cell in the push mode, interrupted by a stop. (A) The raw data, corresponding to the rectangular inset of the trajectory, display the bundle dynamics while the motor stopped rotating. The panels on the left indicate that the pusher slowed down and the bundle underwent a polymorphic transition for a short amount of time ($< 0.05\,\mathrm{ms}$). After that, the flagella bundle reformed and pushed the cell body again (see also Movie S4). (B) Absolute value of the rotational velocity ω for the trajectory. (C) Corresponding speed v data: the stop event is detected from an abrupt slowdown, beginning at time $1.3\,\mathrm{s}$.

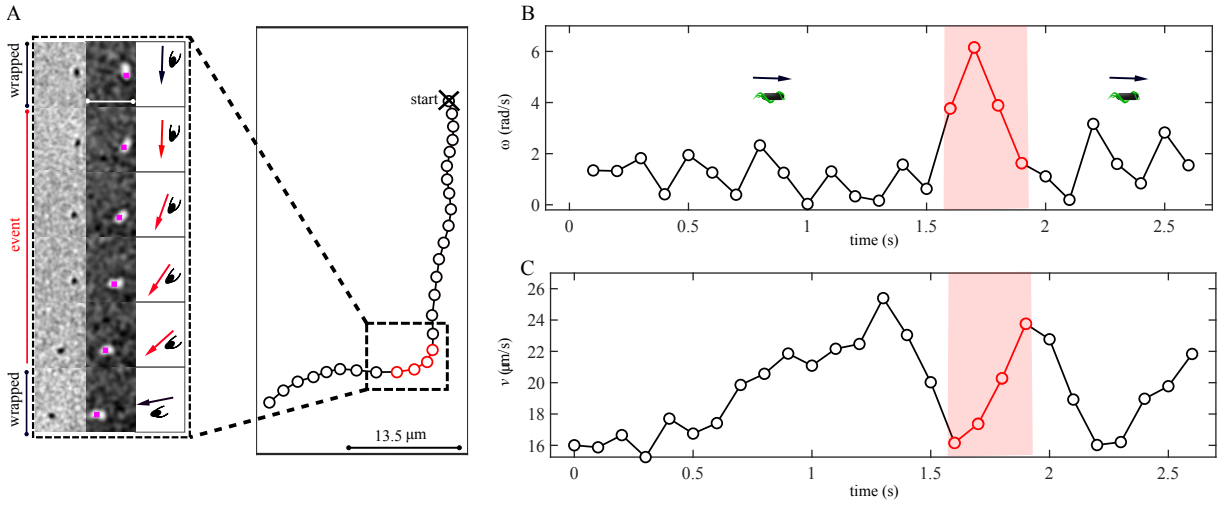

Figure S5: Trajectory of a swimmer in the wrapped mode. (A) The run is interrupted by an event; the direction of motion changes by an angle $\psi_{ww} \approx 90°$. The sequence of raw images suggests that – although the flagellar bundle configuration seems not to have changed – the cell reoriented (see also Movie S5). The high speed movie S9 (snapshots displays in Fig. S7) reveal the mechanistic origin of the reorientation.

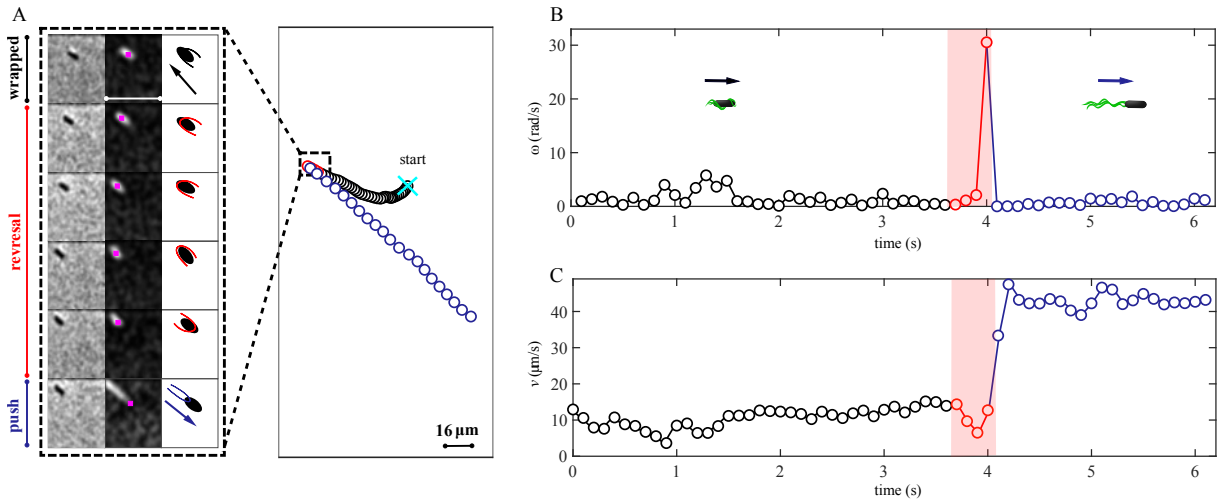

Figure S6: The trajectory illustrates a wrap-push transition. The speed change is clearly visible. (A) Initially, the cell swam in wrapped mode. After a reorientation, it accelerated and the bundle pushes the cell body forward (Movie S6). (B) The time series of the absolute value of the rotational velocity ω shows a peak corresponding to the reversal event. (C) The time series of the speed clearly shows the speed difference of push and wrap mode.

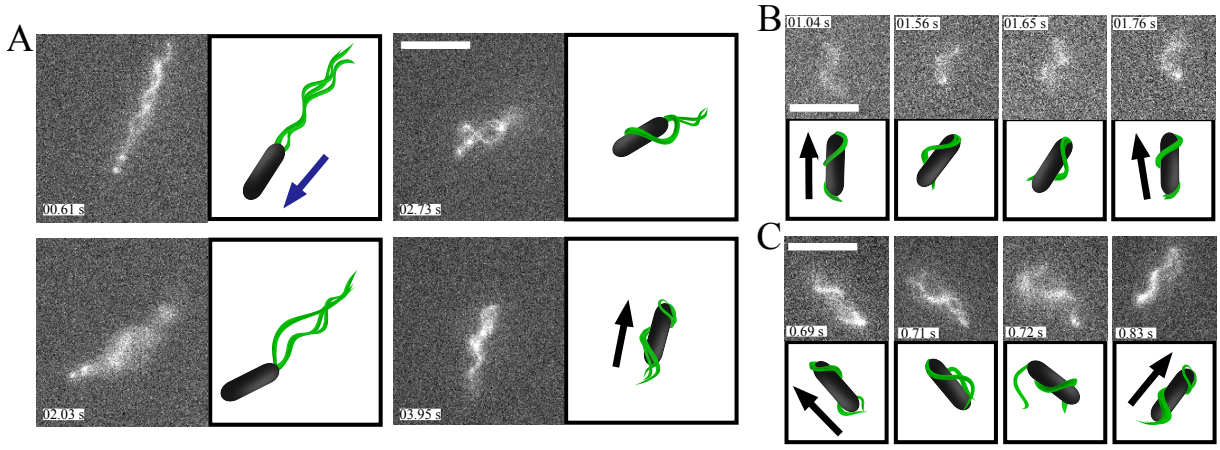

Figure S7: High-speed imaging of the flagellar dynamics during transition. (A) Snapshots of the direct transition from push to wrapped mode (see also Movie S7). The bacterium changed the direction of motion upon reversal when the bundle configuration switched to the wrapped mode. (B) Motor rotation stops during wrapped mode (see also Movie S8). The image sequence in Movie S8 shows that the motor stopped the rotation twice at $0.65\,\mathrm{s}$ and $1.56\,\mathrm{s}$ for about $0.08\,\mathrm{s}$. (C) Wrapped mode interrupted by a stop of the motor rotation, coupled with the disintegration of one filament from the bundle (see also Movie S9). The image series shows, moreover, changes of the direction of motion by roughly $\psi_{ww} \approx 90°$ which is caused by the dissolving bundle dissolving for roughly $0.1\,\mathrm{s}$ (started from time $0.71\,\mathrm{s}$ to $0.82\,\mathrm{s}$). The scale bars indicate $5\,\mu\mathrm{m}$.

S3 Theory of active particles with multi-mode motility

Stochastic dynamics of active particles with multi-mode motility In order to assess the chemotactic efficiency of a bacterial swimmer with multi-mode motility, we developed a descriptive model containing the most relevant physical aspects of the underlying motility pattern, introduced in the following using the example of *P. putida*, cf. Fig. S8.

P. putida self-propels its motion employing a tuft of rotating flagella which are attached to one end of the rod-shaped cell body, thereby enabling persistent active motion at a non-vanishing, characteristic speed (*run motility*). This particular bacterial species exhibits distinct run modes corresponding to different flagellar configurations with respect to the cell body, referred to as *push*, *pull* and *wrapped* mode. For bulk swimming analyzed in this work, we observe significantly less pull-runs compared to the other run modes; that is why this type of run-motility is neglected within the theoretical considerations.

In general, the run-motility in push (P) or wrapped (W) mode may be interrupted for different reasons: the flagellar bundle may disintegrate leading to a change of its conformation, i.e. a transition from push to wrapped mode or vice versa, or the flagellar rotation may be stopped occasionally for short periods of time. As the flagellar activity is not coordinated during those periods, bacteria will not displace themselves actively but only reorient the orientation of their body axis randomly, such that the subsequent run is oriented into a different direction from the preceding one. A typical trajectory will thus be a sequence of runs in push and wrapped mode, interrupted by stop events or transitions from one run mode to another one. In this model, we do not take mechanistic details of run and stop events into account but restrict the model to a descriptive level.

During run phases, bacteria move at a characteristic speed corresponding to the respective run mode – we denoted the speed in push mode v_p and wrapped mode v_w which we assume to be constant. Spatial heterogeneities or fluctuations of the self-propulsion mechanism may induce

rotational noise with the intensities D_p and D_w, respectively, that parametrize the persistence of runs. The occurrence of stop- and transition events as well as their durations are inherently stochastic processes; accordingly, the duration of runs is a random variable. For simplicity, we assume exponential distributions of run times in push and wrapped mode, characterized by the average run times $\tau_p = 1/\kappa_p$ and $\tau_w = 1/\kappa_w$. The rates $\kappa_{p,w}$ determine the probability $\kappa_{p,w}\Delta t$ that a run ends within a time step Δt. In order to account for run-time bias – different run times in dependence of the direction of motion with respect to the chemical gradient – the rates are coupled to the current direction of motion as follows:

$$\kappa_{p,w}(\mathbf{e}) = \lambda_{p,w} - \eta_{p,w}\left(\mathbf{e}\cdot\nabla c\right) = \lambda_{p,w}\Big[1 - \epsilon_{p,w}\left(\mathbf{e}\cdot\nabla c\right)\Big]. \tag{1}$$

Since the run-time is extended upgradient, the corresponding transition rates decrease. Without a chemical gradient, the transition rates are determined by $\lambda_{p,w}$. Here, we consider $\eta_{p,w}$ phenomenological parameters for the run-time bias which could be derived from a microscopic model for the signaling cascade which controls flagellar motor reversals. We note that the bias of run time $\eta_{p,w}$ could, in principle, depend on other motion characteristics such as the speed in the respective run state, for example, which is the case if the underlying model for the run-time bias relies on the memory kernel as discussed in Ref. (*23*), but it is also observed in alternative models describing directed motion in concentration gradients (*24*).

Since a bacterium can be in one of two run modes and both run modes may be interrupted by stops or transitions from one to another, the motility pattern consists of six behavioural states: runs in push (P) and wrapped (W) model, intermittent stops of push (SP) and wrapped (SW) runs as well as transition phases from push to wrap (TP) and vice versa (TW). The motility pattern with all relevant transitions is pictorially represented in Fig. S8(a). Analogous to runs, stop- and transition events have a typical duration. Those times are commonly an order of magnitude smaller than run times. The inverse of all characteristic times are the

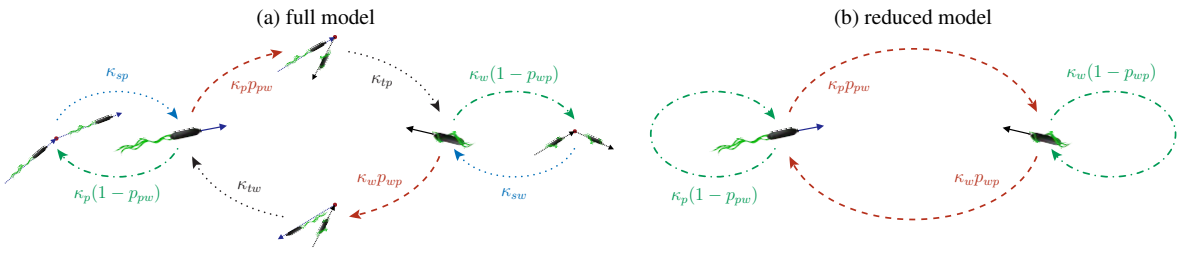

Figure S8: The cartoons are pictorial representations of the transitions between run- and resting states – the dynamics of an active particle with multi-mode motility – corresponding to the master equations (2,5), respectively. *P. putida* has two run states, push (P) and wrap (W), which may be interrupted due to stops (S) of the flagellar driving or their reconfiguration (T) with respect to the cell body. The respective transition rates are denoted by kappa. Model (b) is obtained from the full dynamics (a) assuming that the duration of stop events and flagellar reconfigurations (transitions from wrap to push and vice versa) is much shorter compared to typical run states (see main text for mathematical details of this mapping).

corresponding transition rates, denoted by kappa in Fig. S8(a).

Stops and reconfigurations of flagella imply characteristic distributions for the angle of reorientation of the direction of motion. The dynamics of reorientation is naturally determined by the flagellar activity, however, we are taking a step back from this detailed level of details and describe it instead effectively in terms of a probability distribution. All parameters introduced so far, including typical timescales, run speeds, the persistence of trajectories as well as the probability distribution for reorientations during stop phases can be estimated from experimental data, describing the dynamics of *P. putida*.

The motility pattern depicted in Fig. S8(a) is the representation of a set of master equations that describe the motility in each run state as well as the transitions between them as discussed

above. For the concrete model under consideration, those equations read:

$$\partial_t P_p(\mathbf{r},\mathbf{e},t) = \mathcal{L}_p[P_p] - \kappa_p(\mathbf{e})\,P_p + \int d^d e' [\kappa_{tw} g_{tw}(\mathbf{e}|\mathbf{e}')\,P_{tw}(\mathbf{r},\mathbf{e}',t) + \kappa_{sp} g_{sp}(\mathbf{e}|\mathbf{e}')\,P_{sp}(\mathbf{r},\mathbf{e}',t)], \tag{2a}$$

$$\partial_t P_w(\mathbf{r},\mathbf{e},t) = \mathcal{L}_w[P_w] - \kappa_w(\mathbf{e})\,P_w + \int d^d e' [\kappa_{tp} g_{tp}(\mathbf{e}|\mathbf{e}')\,P_{tw}(\mathbf{r},\mathbf{e}',t) + \kappa_{sw} g_{sw}(\mathbf{e}|\mathbf{e}')\,P_{sw}(\mathbf{r},\mathbf{e}',t)], \tag{2b}$$

$$\partial_t P_{sp}(\mathbf{r},\mathbf{e},t) = (1-p_{pw})\kappa_p(\mathbf{e})\,P_p - \kappa_{sp} P_{sp}, \tag{2c}$$

$$\partial_t P_{sw}(\mathbf{r},\mathbf{e},t) = (1-p_{wp})\kappa_w(\mathbf{e})\,P_w - \kappa_{sw} P_{sw}, \tag{2d}$$

$$\partial_t P_{tp}(\mathbf{r},\mathbf{e},t) = p_{pw}\kappa_p(\mathbf{e})\,P_p - \kappa_{tp} P_{tp}, \tag{2e}$$

$$\partial_t P_{tw}(\mathbf{r},\mathbf{e},t) = p_{wp}\kappa_w(\mathbf{e})\,P_w - \kappa_{tw} P_{tw} \tag{2f}$$

The parameter p_{wp} denotes the probability that – given a run in the wrapped mode ends – it is followed by a push run; an analogous reasoning applies to p_{pw}. Further, the direction of motion in two or three spatial dimensions is determined by the unit vector $\mathbf{e}$. The operator

$$\mathcal{L}_i[P_i] = -v_i \mathbf{e}\cdot\nabla P_i + D_i \Big\{ (d-1)\partial_\mu \Big(e_\mu P_i \Big) + \partial_\mu \partial_\nu \Big[\Big(\delta_{\mu\nu} - e_\mu e_\nu \Big) P_i \Big] \Big\} \tag{3}$$

accounts for self-propelled motion and rotational diffusion during run phases (*38*) in two ($d = 2$) and three ($d = 3$) dimensions, respectively. The components of the unit vector $\mathbf{e}$ were denoted by Greek indices and Einsteins sum convention is implied. The Kronecker symbol $\delta_{\mu\nu}$ equals one for $\mu = \nu$ and zero otherwise.

In line with the experimental observation, we assume that there is no significant particle transport during stop and transition phases. Moreover, isotropic translational diffusion is generally of minor relevance for active swimmers and therefore neglected. Note, however, that the reorientation could alternatively be described by active, rotational diffusion in the states $\{SP, SW, TP, TW\}$. We include this effect into the effective distributions $g_{ij}(\mathbf{e}|\mathbf{e}')$ that describe the probability to obtain the orientation vector $\mathbf{e}$ after a reorientation event given that

the direction of motion was $\mathbf{e}'$ before. This approach allows to simplify the model considerably as discussed next.

As mentioned above, the duration of run phases is much longer compared to stop events or flagellar reconfigurations from wrap to push or vice versa; the experimental data suggest that there is at least one order of magnitude difference. This finding can be used to eliminate Eqs. (2c-2f), thereby reducing to number of equations to two and simplifying the complexity of the problem. We will exploit in this context that the reorientation dynamics during stops is not modeled explicitly but is effectively included in the probability distributions – in this way, the last four equations allow for an immediate analytical solution yielding

$$\begin{aligned} P_{sp}(\mathbf{r},\mathbf{e},t) &= P_{sp}(\mathbf{r},\mathbf{e},0)\, e^{-\kappa_{sp}t} + (1-p_{pw})\kappa_p(\mathbf{e})\int_0^t ds\, P_p(\mathbf{r},\mathbf{e},s)\, e^{-\kappa_{sp}(t-s)} \\ &\approx (1-p_{pw})\frac{\kappa_p(\mathbf{e})}{\kappa_{sp}}\, P_p(\mathbf{r},\mathbf{e},t)\,, \end{aligned} \tag{4a}$$

$$\begin{aligned} P_{sw}(\mathbf{r},\mathbf{e},t) &= P_{sw}(\mathbf{r},\mathbf{e},0)\, e^{-\kappa_{sw}t} + (1-p_{wp})\kappa_w(\mathbf{e})\int_0^t ds\, P_w(\mathbf{r},\mathbf{e},s)\, e^{-\kappa_{sw}(t-s)} \\ &\approx (1-p_{wp})\frac{\kappa_w(\mathbf{e})}{\kappa_{sw}}\, P_w(\mathbf{r},\mathbf{e},t)\,, \end{aligned} \tag{4b}$$

$$\begin{aligned} P_{tp}(\mathbf{r},\mathbf{e},t) &= P_{tp}(\mathbf{r},\mathbf{e},0)\, e^{-\kappa_{tp}t} + p_{pw}\kappa_p(\mathbf{e})\int_0^t ds\, P_p(\mathbf{r},\mathbf{e},s)\, e^{-\kappa_{tp}(t-s)} \\ &\approx p_{pw}\frac{\kappa_p(\mathbf{e})}{\kappa_{tp}}\, P_p(\mathbf{r},\mathbf{e},t)\,, \end{aligned} \tag{4c}$$

$$\begin{aligned} P_{tw}(\mathbf{r},\mathbf{e},t) &= P_{tw}(\mathbf{r},\mathbf{e},0)\, e^{-\kappa_{tw}t} + p_{wp}\kappa_w(\mathbf{e})\int_0^t ds\, P_w(\mathbf{r},\mathbf{e},s)\, e^{-\kappa_{tw}(t-s)} \\ &\approx p_{wp}\frac{\kappa_w(\mathbf{e})}{\kappa_{tw}}\, P_w(\mathbf{r},\mathbf{e},t)\,. \end{aligned} \tag{4d}$$

If the rates in the exponents are high – reflecting that the underlying processes are fast – the initial conditions at $t = 0$ are forgotten quickly; further, one may approximate in the second term under the integrals $P_i(\mathbf{r},\mathbf{e},s) \approx P_i(\mathbf{r},\mathbf{e},t)$ which yields the simplified expressions indicated above. They could equivalently be obtained from the adiabatic elimination $\partial_t P_{sp}(\mathbf{r},\mathbf{e},t) \approx 0$ directly (equivalently for the other quantities P_{sw}, P_{tp} and P_{tw}). Reinserting the closure

relations [Eqs. (4)] into the full dynamics [Eq. (2)] yields the following, simplified description:

$$\partial_t P_p(\mathbf{r},\mathbf{e},t) = \mathcal{L}_p[P_p] - \kappa_p(\mathbf{e})\,P_p + \int d^d e' [p_{wp}\kappa_w(\mathbf{e}')\,g_{tw}(\mathbf{e}|\mathbf{e}')\,P_w(\mathbf{r},\mathbf{e}',t) + (1-p_{pw})\kappa_p(\mathbf{e}')\,g_{sp}(\mathbf{e}|\mathbf{e}')\,P_p(\mathbf{r},\mathbf{e}',t)], \tag{5a}$$

$$\partial_t P_w(\mathbf{r},\mathbf{e},t) = \mathcal{L}_w[P_w] - \kappa_w(\mathbf{e})\,P_w + \int d^d e' [p_{pw}\kappa_p(\mathbf{e}')\,g_{tp}(\mathbf{e}|\mathbf{e}')\,P_p(\mathbf{r},\mathbf{e}',t) + (1-p_{wp})\kappa_w(\mathbf{e}')\,g_{sw}(\mathbf{e}|\mathbf{e}')\,P_w(\mathbf{r},\mathbf{e}',t)]. \tag{5b}$$

These equations represent a reduced model where the stop and transition phases were integrated out; it is graphically represented in Fig. S8(b). This model is the basis for the analysis of the chemotactic efficiency for the motion pattern of *P. putida*.

Large-scale transport properties – drift-diffusion approximation The models for the multi-mode motility of *P. putida* introduced above, cf. Eqs. (2,5), are of the general form

$$\partial_t \mathcal{P}_i(\mathbf{r},\mathbf{e},t) = -\,v_i\mathbf{e}\cdot\nabla\mathcal{P}_i + D_i\Big\{(d-1)\partial_\mu\Big(e_\mu\mathcal{P}_i\Big) + \partial_\mu\partial_\nu\Big[\Big(\delta_{\mu\nu}-e_\mu e_\nu\Big)\mathcal{P}_i\Big]\Big\} - \sum_j\Big\{\kappa_{ij}(\mathbf{e})\mathcal{P}_i - \int d^d e'\,\kappa_{ji}(\mathbf{e}')\,g_{ji}(\mathbf{e}|\mathbf{e}')\mathcal{P}_j(\mathbf{r},\mathbf{e}',t)\Big\}. \tag{6}$$

The distribution function $\mathcal{P}_i(\mathbf{r},\mathbf{e},t)$ denotes the density of particles at position $\mathbf{r}$ moving into the direction $\mathbf{e}$ at time t in motility state i. In order to simplify the notation, individual motility states will be enumerated as indicated by Latin letters – let $\kappa_{ij}(\mathbf{e})$ be the rate for the transition from state i to j that may generally depend on the direction of motion within a chemical gradient (run-time bias). We expand all field-dependent rates into a Fourier series keeping the first nontrivial order only:

$$\kappa_{ij}(\mathbf{e}) \approx \lambda_{ij} - \eta_{ij}\mathbf{e}\cdot\nabla c. \tag{7}$$

This is, at the same time, a Taylor expansion in spatial gradients to first order that is justified as the variation of the chemical field over spatial scales that a bacterium traverses within one single run is small and, thus, it is well approximated by a linear gradient. Accordingly, we will keep first order terms in ∇c only in the following. Beyond that the experimental situation is such that the chemical gradient is indeed linear.

The purpose of this section is to give mathematical details on the derivation of the drift-diffusion approximation from the full dynamics that was used in the main text to address the chemotactic efficiency of bacterial swimmers with multi-mode motility. It will be argued below that the total density

$$\rho(\mathbf{r},t) = \sum_j \int d^d e \, \mathcal{P}_j(\mathbf{r},\mathbf{e},t) \tag{8}$$

approximately fulfils a Fokker-Planck equation of the form

$$\partial_t \rho \simeq -\nabla \cdot \Big[\mu \, (\nabla c) \, \rho \Big] + D \Delta \rho \tag{9}$$

on large scales in the long-time limit. The average chemotactic drift velocity is given by $\mathbf{v}_d = \mu \nabla c$ and D is the long-time diffusion coefficient. The effective transport coefficients μ and D are functions of the underlying motility pattern, i.e. the transition rates as well as the motion characteristics of individual runs, such as speed and persistence.

As a first step, we perform an order-parameter expansion of the master equation (6) beginning with the densities

$$\rho_i(\mathbf{r},t) = \int d^d e \, \mathcal{P}_i(\mathbf{r},\mathbf{e},t) \tag{10}$$

that determine the local density of swimmers in a certain motion state (index i). Their dynamics

is obtained by integrating Eq. (6) over all orientations $\mathbf{e}$:

$$\partial_t \rho_i(\mathbf{r},t) = -v_i \nabla\cdot\mathbf{m}_i(\mathbf{r},t) - \sum_j \int d^d e \left\{\kappa_{ij}(\mathbf{e})\mathcal{P}_i(\mathbf{r},\mathbf{e},t) - \kappa_{ji}(\mathbf{e})\mathcal{P}_j(\mathbf{r},\mathbf{e},t)\right\} \tag{11a}$$

$$= -v_i \nabla\cdot\mathbf{m}_i(\mathbf{r},t) - \sum_j \Big[\lambda_{ij}\rho_i - \lambda_{ji}\rho_j\Big] + \sum_j \Big[\eta_{ij}\mathbf{m}_i\cdot\nabla c - \eta_{ji}\mathbf{m}_j\cdot\nabla c\Big]. \tag{11b}$$

To obtain the second line, we inserted the linearized rates given by Eq. (7). Upon summation over all i, the last terms cancel out by symmetry such that the density dynamics is determined by

$$\partial_t \rho(\mathbf{r},t) = -\sum_i v_i \nabla\cdot\mathbf{m}_i(\mathbf{r},t). \tag{12}$$

Accordingly, particle transport within individual states is determined by the momentum flux $\mathbf{w}_i = v_i\mathbf{m}_i$ where

$$\mathbf{m}_i(\mathbf{r},t) = \int d^d e\, \mathbf{e}\mathcal{P}_i(\mathbf{r},\mathbf{e},t) = \rho_i \langle\mathbf{e}\rangle_i \tag{13}$$

is proportional to the local mean orientation of particles $\langle\mathbf{e}\rangle_i$ in state i. The dynamics of the densities is thus not closed but a hierarchy of modes will be obtained – the densities $\rho_i(\mathbf{r},t)$ are coupled to the momentum fluxes which depend, in turn, on other order parameters. We will use the fact that the large-scale, long-time dynamics of the total density $\rho(\mathbf{r},t)$ is only determined by particle transport [cf. Eq. (12)] and, hence, is much slower compared to the dynamics of $\mathbf{m}_i(\mathbf{r},t)$, for example, that evolve on a timescale of the inverse transition rates λ_{ij}. Mathematically speaking, the total density is a slow mode within the hierarchy of order parameter equations which is why the dynamics of all other order parameter fields are enslaved by the density in the long-time limit. One may equivalently consider this projection of order-parameter equations onto the slow mode (density ρ) a *local equilibrium ansatz* as shown below.

In order to find a closure relation for Eq. (12) – an expression for all fields $\mathbf{m}_i$ in terms of the total density ρ – we consider the dynamics of the fields $\mathbf{m}_i(\mathbf{r},t)$, obtained by multiplication

of the master equations [Eqs. (6)] with $\mathbf{e}$ and subsequent integration of the direction of motion:

$$\partial_t \mathbf{m}_i(\mathbf{r},t) = -v_i \nabla\cdot\mathcal{T}_i - D_i(d-1)\mathbf{m}_i - \sum_j \int d^d e\, \mathbf{e}\Big\{\kappa_{ij}(\mathbf{e})\mathcal{P}_i(\mathbf{r},\mathbf{e},t) - \kappa_{ji}(\mathbf{e})\Gamma_{ji}\mathcal{P}_j(\mathbf{r},\mathbf{e},t)\Big\}. \tag{14}$$

In the last term, we used the rotational symmetry of the reorientation statistics $g_{ji}(\mathbf{e}|\mathbf{e}') = \delta(1-|\mathbf{e}|)\, f_{ji}(\mathbf{e}\cdot\mathbf{e}')$ to simplify

$$\int d^d e\, \mathbf{e}\, g_{ji}(\mathbf{e}|\mathbf{e}') = \mathbf{e}'\langle \mathbf{e}\cdot\mathbf{e}'\rangle_{ji} = \mathbf{e}'\langle\cos\psi\rangle_{ji} = \mathbf{e}'\Gamma_{ji} \tag{15}$$

and denoted $\Gamma_{ji} = \langle\cos\psi\rangle_{ji}$ the mean cosine of the reorientation angle for a specific transition from state j to i. Inserting the field dependence of the transition rates again [Eq. (7)], the integral on the right hand side of Eq. (14) can be calculated explicitly:

$$\begin{aligned}\partial_t \mathbf{m}_i(\mathbf{r},t) = &-v_i\nabla\cdot\mathcal{T}_i - D_i(d-1)\mathbf{m}_i \\ &- \sum_j \Big[\lambda_{ij}\mathbf{m}_i - \lambda_{ji}\Gamma_{ji}\mathbf{m}_j\Big] + \sum_j \Big[\eta_{ij}\mathcal{T}_i\cdot\nabla c - \eta_{ji}\Gamma_{ji}\mathcal{T}_j\cdot\nabla c\Big].\end{aligned} \tag{16}$$

The dynamics of the orientation fields $\mathbf{m}_i(\mathbf{r},t)$ is coupled to the next higher, matrix-valued order parameter

$$\{\mathcal{T}_i(\mathbf{r},t)\}_{\mu\nu} = \int d^d e\, e_\mu e_\nu \mathcal{P}_i(\mathbf{r},\mathbf{e},t)\,. \tag{17}$$

Since the dynamics of the orientation fields $\mathbf{m}_i$ is fast compared to the density dynamics, they can be adiabatically eliminated just like it was done explicitly in the context of the derivation of a reduced model from the full dynamics: we approximate $\partial_t \mathbf{m}_i \approx 0$ and solve Eq. (16) for $\mathbf{m}_i$ yielding

$$\mathbf{m}_i(\mathbf{r},t) \approx -\sum_j \left\{\mathcal{M}^{-1}\right\}_{ij} v_j \nabla\cdot\mathcal{T}_j - \sum_{jk}\left\{\mathcal{M}^{-1}\right\}_{ij}\mathcal{O}_{jk}\mathcal{T}_k\cdot\nabla c \tag{18}$$

where the matrices $\mathcal{M}$ and $\mathcal{O}$ with the entries

$$\mathcal{M}_{ij} = \delta_{ij}D_i(d-1) + \left[\delta_{ij}\sum_k\Big(\lambda_{jk}\Big) - \lambda_{ji}\Gamma_{ji}\right], \quad \mathcal{O}_{ij} = -\delta_{ij}\Big(\sum_k \eta_{ik}\Big) + \eta_{ji}\Gamma_{ji} \tag{19}$$

were introduced for convenience. If Eq. (18) is inserted into the transport equation for the density [Eq. (12)], the structure of the final equation [cf. Eq. (9)] can already be conjectured: there is a second order derivative that will yield the diffusion term and a drift term that includes gradients of the external field (∇c). What is left to be done is to express the tensors $\mathcal{T}_i$ in terms of the density ρ. To the order which we work in – first order in spatial gradients with the aim of the reduction to a drift-diffusion approximation – it is sufficient to consider these tensors $\mathcal{T}_i$ spatially homogeneous and field independent because all additional contributions would introduce higher order terms. Due to the same reasoning, the last term in Eq. (11) containing the products $\mathbf{m}_i \cdot \nabla c$ is approximately zero as it would produce nonlinear contributions. The field independent, spatially homogeneous dynamics of the tensors $\mathcal{T}_i$ is determined by

$$\begin{aligned}\partial_t \{\mathcal{T}_i\}_{\mu\nu} \approx & -2dD_i \{\mathcal{T}_i\}_{\mu\nu} + 2D_i\rho_i\delta_{\mu\nu} \\ & - \sum_j \int d^d e\, e_\mu e_\nu \left\{ \kappa_{ij}(\mathbf{e}) \mathcal{P}_i(\mathbf{r}, \mathbf{e}, t) - \int d^d e' \kappa_{ji}(\mathbf{e}') g_{ji}(\mathbf{e}|\mathbf{e}') \mathcal{P}_j(\mathbf{r}, \mathbf{e}', t) \right\}. \end{aligned} \tag{20}$$

Similarly to the reasoning before, we first calculate the conditional average

$$\int d^d e\, e_\mu e_\nu g_{ji}(\mathbf{e}|\mathbf{e}') = \frac{d\Lambda_{ji} - 1}{d-1} e'_\mu e'_\nu + \frac{1 - \Lambda_{ji}}{d-1} \delta_{\mu\nu} \tag{21}$$

assuming unbiased reorientation statistics with respect to the original direction of motion, where $\Lambda_{ji} = \langle \cos^2 \psi \rangle_{ji}$ is the squared average cosine of the reorientation angle for each transition from j to i as indicated and d is the spatial dimension. Inserting into the equation above allows for a simplification as follows:

$$\begin{aligned}\partial_t \{\mathcal{T}_i\}_{\mu\nu} = & -2dD_i \{\mathcal{T}_i\}_{\mu\nu} + 2D_i\rho_i\delta_{\mu\nu} \\ & - \sum_j \left[\lambda_{ij} \{\mathcal{T}_i\}_{\mu\nu} - \frac{d\Lambda_{ji} - 1}{d-1} \lambda_{ji} \{\mathcal{T}_j\}_{\mu\nu} \right] + \sum_j \frac{1 - \Lambda_{ji}}{d-1} \delta_{\mu\nu} \lambda_{ji} \rho_j. \end{aligned} \tag{22}$$

The unique stationary solution of this equation obtained via adiabatic elimination, $\partial_t \{\mathcal{T}_i\}_{\mu\nu} \approx 0$, is given by the rather simple expression

$$\{\mathcal{T}_i\}_{\mu\nu} = \delta_{\mu\nu} \frac{\rho_i}{d} \tag{23}$$

if the densities ρ_i fulfil the condition

$$0 = \sum_j \Big[\lambda_{ij}\rho_i - \lambda_{ji}\rho_j\Big]. \tag{24}$$

Note that a term of similar type appears on the right hand side of the density dynamics [Eq. (11b)]: it has the structure of a master equation that describes the stationary state of a system where λ_{ij} are the rates for transitions from states i to j, and ρ_i are the populations of the respective states. Accordingly, it reflects the assumption of *local equilibrium* mentioned earlier. We denote the solution by $\rho_i = \rho P_i$ where

$$\sum_j \mathcal{Q}_{ij}P_j = 0, \quad \mathcal{Q}_{ij} = \delta_{ij}\Big(\sum_k \lambda_{ik}\Big) - \lambda_{ji}, \quad \sum_j P_j = 1. \tag{25}$$

Mathematically speaking, $\mathbf{P}$ is the eigenvector corresponding to eigenvalue zero of the matrix $\mathcal{Q}$. Its components P_i correspond to the probability that a particle is found in a certain motion state i in a spatially homogeneous system ($\nabla c = 0$).

This final step completes the drift-diffusion approximation. The expression for the transport coefficients μ and D are eventually obtained by inserting $\{\mathcal{T}_i\}_{\mu\nu} = \delta_{\mu\nu}P_i\rho/d$ into the expression for $\mathbf{m}_i$ [Eq. (18)] and the resulting expression into the density dynamics [Eq. (12)] yielding

$$\mu = -\frac{1}{d}\sum_{ijk} v_i\big\{\mathcal{M}^{-1}\big\}_{ij}\mathcal{O}_{jk}P_k, \quad D = \frac{1}{d}\sum_{ij} v_i v_j\big\{\mathcal{M}^{-1}\big\}_{ij}P_j. \tag{26}$$

Given a certain motility pattern characterized by the transition rates κ_{ij}, the speeds v_i and rotational diffusion coefficients D_i as well as the reorientation statistics, more precisely the mean cosine of the reorientation angle $\Gamma_{ij} = \langle\cos\psi\rangle_{ij}$ for each transition, these formulae allow to calculate the chemotactic response and the diffusion coefficient for an active particle with multimode motility pattern within a drift-diffusion framework: based on Eq. (19), the matrices $\mathcal{M}$ and $\mathcal{O}$ are constructed, the matrix $\mathcal{M}$ has to be inverted and the components of the vector $\mathbf{P}$ are found from the null space of matrix $\mathcal{Q}$ defined in Eq. (25). Below, this procedure is explicitly applied to the motility pattern observed for *P. putida*.

We highlight that the spatial dimension is only included in the prefactor $1/d$ but it is not changing the parameter dependence of transport coefficients structurally. Hence, all qualitative results deduced from the drift-diffusion approximation are de facto dimension-independent. Further, we note that the approach outlined above describes adaptive chemotaxis strategies as the reorientation rates κ_{ij} couple to the gradient orientation only, but they are independent of the value of the local fields c. That is why the diffusion coefficient D is a constant and, moreover, independent of the external field. The same value for the diffusion coefficients is obtained in homogeneous systems without chemical gradients, discussed in (*7*).

Drift-diffusion approximation for *P. putida* In this appendix section, we list some mathematical details concerning the application of the drift-diffusion approximation, as discussed in the previous section, to the motility pattern displayed by *P. putida*. For simplicity, we neglect the finite duration of stops and flagellar reconfigurations as they occur on timescales that are considerably faster compared to the mean run time; our data suggest that there is at least one order of magnitude difference. Accordingly, we apply the drift-diffusion approximation to the dynamics reflected by Eqs. (5), pictorially represented in Fig. S8(b).

For the following theoretical considerations, we assume that both the run time in push and wrapped mode are dependent on the actual direction of motion with respect to the chemical gradient, i.e. both are *chemotactic modes*:

$$\kappa_p(\mathbf{e}) = \lambda_p - \eta_p(\mathbf{e}\cdot\nabla c)\,, \quad \kappa_w(\mathbf{e}) = \lambda_w - \eta_w(\mathbf{e}\cdot\nabla c)\,. \tag{27}$$

The rates $\lambda_{p,w}$ are the inverse run time in push (p) and wrapped (w) mode in spatially homogeneous environments. The coupling of the run time to the chemical gradient is determined by the parameters $\eta_{p,w}$: the run time is enhanced upgradient (taxis towards a chemoattractant) for $\eta_{p,w} > 0$, implying that the corresponding rate is decreased. It reflects the actual run-time bias – the difference of mean run times up- and downgradient – measured experimentally.

In order to simplify the notation, we index the push and wrapped run state by 1 and 2, respectively. The relevant transition matrices then read as follows:

$$\lambda = \begin{pmatrix} \lambda_p(1-p_{pw}) & \lambda_p p_{pw} \\ \lambda_w p_{wp} & \lambda_w(1-p_{wp}) \end{pmatrix}, \quad \eta = \begin{pmatrix} \eta_p(1-p_{pw}) & \eta_p p_{pw} \\ \eta_w p_{wp} & \eta_w(1-p_{wp}) \end{pmatrix}. \tag{28}$$

The long-time transport properties, parameterized by μ and D, are obtained by insertion into the general expressions discussed in the previous section.

We first look at the effective chemotactic drift velocity $\mathbf{v}_d = \mu\nabla c$. Since the expressions are rather complicated, a couple of abbreviations needs to be introduced. Let

$$P_p = \frac{\lambda_w p_{wp}}{\lambda_p p_{pw} + \lambda_w p_{wp}}, \quad P_w = \frac{\lambda_p p_{pw}}{\lambda_p p_{pw} + \lambda_w p_{wp}} \tag{29}$$

be the probabilities to find a bacterial swimmer in the push or wrapped mode in the stationary state that is obtained as the kernel of the matrix $\mathcal{Q}$ via $\mathcal{Q}\cdot\mathbf{P} = 0$ and $P_p + P_w = 1$, as previously defined in Eq. (25). Further, we denote μ as a sum of two parts

$$\mu = \mu_p\eta_p + \mu_w\eta_w, \tag{30}$$

where μ_p is the chemotactic response due to a potential run-time bias in the push mode and μ_w is the corresponding response function in the wrapped mode. Since the theory considers dependencies in the chemical field to first order, the transport coefficient μ is directly proportional to the relative run-time bias $\eta_{p,w}$. The corresponding prefactors, referred to as *response functions*, are given by

$$\mu_p = \frac{P_p}{d}\cdot\frac{v_p\mathcal{D}_w\left[1-\Gamma_{pp}\left(1-p_{pw}\right)\right] - v_w D_p p_{pw}\Gamma_{pw} - v_p\Gamma_{pw}\Gamma_{wp}\lambda_w p_{pw}p_{wp}}{\mathcal{D}_p\mathcal{D}_w - \Gamma_{pw}\Gamma_{wp}\lambda_p\lambda_w p_{pw}p_{wp}}, \tag{31a}$$

$$\mu_w = \frac{P_w}{d}\cdot\frac{v_w\mathcal{D}_p\left[1-\Gamma_{ww}\left(1-p_{wp}\right)\right] - v_p D_w p_{wp}\Gamma_{wp} - v_w\Gamma_{pw}\Gamma_{wp}\lambda_p p_{pw}p_{wp}}{\mathcal{D}_p\mathcal{D}_w - \Gamma_{pw}\Gamma_{wp}\lambda_p\lambda_w p_{pw}p_{wp}} \tag{31b}$$

where we abbreviated the effective rotational diffusion coefficients

$$\mathcal{D}_p = D_p + \lambda_p\big[1-\Gamma_{pp}\left(1-p_{pw}\right)\big], \tag{32a}$$

$$\mathcal{D}_w = D_w + \lambda_w\big[1-\Gamma_{ww}(1-p_{wp})\big]. \tag{32b}$$

The chemotactic response consists of two parts: the run-time bias in the respective run modes, η_p and η_w, and the corresponding response functions μ_p and μ_w, respectively. The run-time bias depends on the way how a bacterium senses extra-cellular chemical concentrations as well as the internal signaling cascade controlling flagellar activity. As we do not address the biochemistry of the chemotaxis pathway, we do not explain the origin of the run-time bias $\eta_{p,w}$ but rather consider it as given, for example by the experimental investigation. What the analysis provides is the response functions $\mu_{p,w}$ that do basically depend on how a bacterium moves in the respective run modes, its speed and persistence as well as the reorientation statistics upon stopping or transitions from one run mode to another. Given a certain run-time bias, a specific motility pattern determines the efficiency of a chemotactic response.

Using the abbreviations introduced above, the effective diffusion coefficient reads

$$D = \frac{1}{d} \cdot \left[P_p \cdot \frac{v_p^2 \mathcal{D}_w + v_p v_w \lambda_p p_{pw} \Gamma_{pw}}{\mathcal{D}_p \mathcal{D}_w - \Gamma_{pw} \Gamma_{wp} \lambda_p \lambda_w p_{pw} p_{wp}} + P_w \cdot \frac{v_w^2 \mathcal{D}_p + v_p v_w \lambda_w p_{wp} \Gamma_{wp}}{\mathcal{D}_p \mathcal{D}_w - \Gamma_{pw} \Gamma_{wp} \lambda_p \lambda_w p_{pw} p_{wp}} \right]. \tag{33}$$

It is instructive to see in this regard how these expression simplify if no transitions in between swim modi occurred. For $p_{pw} \to 0$, a bacterium would stay all the time in the push run mode, interrupted by stop events at a rate λ_p. The resulting transport coefficients then read

$$\mu_p = \frac{1}{d} \cdot \frac{v_p \lambda_p \left(1 - \Gamma_{pp}\right)}{\mathcal{D}_p} = \frac{1}{d} \cdot \frac{v_p \lambda_p \left(1 - \Gamma_{pp}\right)}{D_p + \lambda_p \big(1 - \Gamma_{pp}\big)}, \tag{34}$$

and, trivially, $\mu_w = 0$ as well as

$$D = \frac{1}{d} \cdot \frac{v_p^2}{\mathcal{D}_p} = \frac{1}{d} \cdot \frac{v_p^2}{D_p + \lambda_p \big(1 - \Gamma_{pp}\big)}. \tag{35}$$

The equivalent expressions for $p_{wp} \to 0$ are obtained by interchanging indices for push and wrapped mode: $p \leftrightarrow w$. Those expressions may by considered the *pure* cases in the sense that only run mode is accessible, interrupted by reorientation events. The structure of the diffusion coefficient in these limits is typical: it is determined by the squared speed times the persistence time, given by the inverse effective rotational diffusion coefficient. The effective rotational

diffusion incorporates the actual rotational diffusion, reorientation rates as well as the statistics of the reorientation angle. As a last point, we note that the spatial dimensionality does not affect any result discussed in this work qualitatively as it contributes a trivial prefactor d^{-1} to the response functions [Eq. (31)] and the diffusion coefficient [Eq. (33)].

Relevance of the pull-run-mode We note that the response functions μ_p and μ_w of the pull and wrapped states discussed in the main text are proportional to the probabilities $P_{p,w}$ to find a bacterium in the respective run state, cf. Eq. (31). By studying an extended version of the model including pull runs, that was introduced in Ref. (*7*), we convinced ourselves that the full response function can be written as

$$\mu = \mu_p \eta_p + \mu_w \eta_w + \mu_l \eta_l,$$

to first order in gradients, cf. Eq. (3) in the main text. Here, the index l denotes the pull state. Furthermore, each of the response functions is proportional to the probability to find the bacterium in the respective swimming mode,

$$\mu_p \propto P_p, \quad \mu_w \propto P_w, \quad \mu_l \propto P_l,$$

i.e. the response functions are proportional to the relative fraction of time a bacterium spends in each run state. We checked that μ_l tends to zero if the life time of the pull state tends to zero, consistently. Since we observed only very few pull runs in our study (around 2% as shown in Fig. 1), we can indeed neglect the pull state within our modeling study as they are irrelevant for the long-time, large-scale transport properties.

Chemotaxis in disordered environments In the main text, the chemotactic efficiency of bacterial swimmers with multi-mode motility in disordered environments is discussed. Mathematical details on the modeling are given in this section.

We include collisions of bacteria with obstacles into the model of swimmers with multi-mode motility, as schematically represented in Fig. S9: compared to Fig. S8, there are two additional transition pathways symbolizing collision events. As before, the duration of stop, transition and collision events is not taken into account for simplicity. Mathematically speaking, we describe the dynamics in heterogeneous environments within the same framework introduced above by

$$\begin{aligned}\partial_t P_p(\mathbf{r},\mathbf{e},t) &= \mathcal{L}_p[P_p] + \mathcal{L}_c[P_p] - \kappa_p(\mathbf{e})P_p \\ &\quad + \int d^d e' [p_{wp}\kappa_w(\mathbf{e}')g_{tw}(\mathbf{e}|\mathbf{e}')P_w(\mathbf{r},\mathbf{e}',t) + (1-p_{pw})\kappa_p(\mathbf{e}')g_{sp}(\mathbf{e}|\mathbf{e}')P_p(\mathbf{r},\mathbf{e}',t)],\end{aligned} \tag{36a}$$

$$\begin{aligned}\partial_t P_w(\mathbf{r},\mathbf{e},t) &= \mathcal{L}_w[P_w] + \mathcal{L}_c[P_w] - \kappa_w(\mathbf{e})P_w \\ &\quad + \int d^d e' [p_{pw}\kappa_p(\mathbf{e}')g_{tp}(\mathbf{e}|\mathbf{e}')P_p(\mathbf{r},\mathbf{e}',t) + (1-p_{wp})\kappa_w(\mathbf{e}')g_{sw}(\mathbf{e}|\mathbf{e}')P_w(\mathbf{r},\mathbf{e}',t)],\end{aligned} \tag{36b}$$

where the collision operator

$$\mathcal{L}_c[P_i] = -\kappa_i^{(c)}\left[P_i(\mathbf{r},\mathbf{e},t) - \int d^d e' g_c(\mathbf{e}|\mathbf{e}')P_i(\mathbf{r},\mathbf{e}',t)\right] \tag{37}$$

with $\kappa_i^{(c)} = v_i\rho_0\sigma$ was added in the respective motility states. The reorientation of the direction of motion induced by collisions is described by the probability density function $g_c(\mathbf{e}|\mathbf{e}')$.

Based on Eqs. (36,37), we performed a drift-diffusion approximation to obtain expressions for the long-time chemotactic drift velocity $\mathbf{v}_d \simeq \mu\nabla c$ as well as the effective diffusion coefficient D. The derivation follows the steps discussed in detail before. We find that the relevant transport coefficients μ and D are structurally identical to Eqs. (31,33) discussed before – collisions with obstacles will effectively renormalize the rotational diffusion coefficients:

$$D_p \to D_p + v_p\rho_0\sigma(1-\Gamma_c), \tag{38a}$$

$$D_w \to D_w + v_w\rho_0\sigma(1-\Gamma_c). \tag{38b}$$

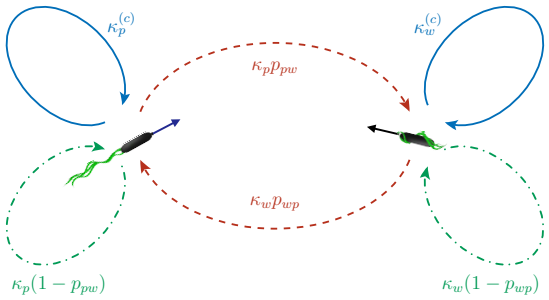

Figure S9: Generalization of the motility pattern of *P. putida* with multi-mode motility, cf. Fig. S8, including collisions with obstacles at rates $\kappa_p^{(c)}$ and $\kappa_w^{(c)}$ in push and wrap mode, respectively. Collisions are assumed to induce a random change of the direction of motion.

The relative increase of rotational diffusion is, however, proportional to the speed in the respective run state and, thus, different for push and wrapped run mode as collisions are more likely to occur for large speeds in a given time interval. The factor $\Gamma_c = \langle \cos\psi \rangle_c$ is the mean cosine of the reorientation angle upon collisions of bacteria with obstacles.

In the main text, we discussed the chemotactic drift coefficients μ_p and μ_w as a function of the mean free path, i.e. the characteristic distance $l_c = 1/(\rho_0\sigma)$ in between obstacles. For low obstacles densities, the mean free path diverges and, thus, the drift coefficients reduce to the expressions in a homogeneous medium without obstacles as can be seen from Eqs. (38). In the opposite limit of high obstacles densities corresponding to high collisions rates with obstacles or, equivalently, small mean-free path lengths $l_c \to 0$, the drift coefficients reduce to the following expressions:

$$\mu_p \simeq \frac{P_p}{d(1-\Gamma_c)} \cdot \frac{\kappa_w^{(c)} v_p \left[1 - \Gamma_{pp}(1-p_{pw})\right] - \kappa_p^{(c)} v_w \Gamma_{pw} p_{pw}}{\kappa_p^{(c)} \kappa_w^{(c)}} = \frac{P_p}{d} \cdot \frac{1-\bar{\Gamma}_p}{1-\Gamma_c} \cdot l_c + \mathcal{O}\big(l_c^2\big), \tag{39a}$$

$$\mu_w \simeq \frac{P_w}{d(1-\Gamma_c)} \cdot \frac{\kappa_p^{(c)} v_w \left[1 - \Gamma_{ww}(1-p_{wp})\right] - \kappa_w^{(c)} v_p \Gamma_{wp} p_{wp}}{\kappa_p^{(c)} \kappa_w^{(c)}} = \frac{P_w}{d} \cdot \frac{1-\bar{\Gamma}_w}{1-\Gamma_c} \cdot l_c + \mathcal{O}\big(l_c^2\big). \tag{39b}$$

First of all, we see from these expressions that the chemotactic performance vanishes in the

limit of high obstacles densities ($l_c \to 0$), consistently. Further, the speeds cancel from the expressions in this limit because the collisions rates $\kappa_i^{(c)}$ are proportional to the speeds itself – in contrast to the situation without obstacles, increasing the speed of runs does not imply a higher chemotaxis efficiency because collisions with obstacles become more frequent. The transport coefficients μ_p and μ_w are rather determined by purely geometric properties of the trajectories: the coefficients $\bar{\Gamma}_p = \Gamma_{pp}(1 - p_{pw}) + \Gamma_{pw}p_{pw}$ and $\bar{\Gamma}_w = \Gamma_{ww}(1 - p_{wp}) + \Gamma_{wp}p_{wp}$ are the weighted average of the reorientation angle in the push and in the wrapped mode, respectively.

S4 Details on data analysis and parameter inference

Parametric maximum likelihood inference of the run-time statistics In order to substantiate the statistical analysis of the run-time statistics discussed in the main text (cf. Fig. 3), which is based on a (numerical) non-parametric maximum likelihood estimate (*15*), we additionally present in this appendix a parametric maximum likelihood approach. This will allow us to quantify the statistical significance of differences between the up- and downgradient run-time distributions in the push and wrapped swimming modes. As a model for the run time distribution, we use the Weibull distribution

$$\psi_x(t) = \zeta k(\zeta t)^{k-1} e^{-(\zeta t)^k}. \tag{40}$$

This probability density function has two parameters: k parametrizes the shape of the distribution and ζ determines the characteristic timescale. We chose this distribution because it is a rather flexible model in the sense that in contains several important limiting cases. For $k = 1$, it reduces to an exponential distribution. Therefore, the maximum likelihood analysis provides a direct test of how close the run-time distributions are to an exponential distribution, which is implicitly assumed in the active particle model. Moreover, the skewness of this distribution vanishes for $k \approx 3.6$ where it becomes bell-shaped, similar to a Gaussian distribution.

The observed run-times have to be classified into four categories as detailed below (*15*). There are runs which begin and end with a turn or stop event; the statistics of these follows the probability density function $\psi_x(t)$. We abbreviate these run-times as x_i with $i = 1, 2, \ldots, n_X$. Different types of censoring can appear if bacteria enter or leave the focal imaging plane during a run, such that the observation of a run does not start or end with a turn or stop: run times where the beginning was not observed but the end is observed are abbreviate by y_i ($i = 1, 2, \ldots, n_Y$); those where only the beginning but not the end was observed are referred to as z_i ($i = 1, 2, \ldots, n_Z$); finally, the observation time of runs which are censored on both sides are called w_i ($i = 1, 2, \ldots, n_W$). Accordingly, the total number of runs is $N = n_X + n_Y + n_Z + n_W$. Distinguishing these different types of runs is important as they contribute differently to the likelihood function

$$\mathcal{L} = \left(\prod_{i=1}^{n_X} \psi_x(x_i) \right) \cdot \left(\prod_{j=1}^{n_Y} \psi_y(y_j) \right) \cdot \left(\prod_{l=1}^{n_Z} \psi_z(z_l) \right) \cdot \left(\prod_{m=1}^{n_W} \psi_w(w_m) \right) \tag{41}$$

where

$$\psi_y(t) = \frac{\zeta}{\Gamma(1+1/k)} e^{-(\zeta t)^k}, \quad \psi_z(t) = e^{-(\zeta t)^k}, \quad \psi_w(t) = \frac{\Gamma\big(1/k, (\zeta t)^k\big)}{\Gamma(1/k)}, \tag{42}$$

which were derived from the actual run-time distribution [Eq. (40)] applying renewal theory, cf. Ref (*39*). Loosely speaking, an observation of a run of type z with the duration z_i contains the information that the run-time was equal or longer than z_i, which is why $\psi_z(t)$ is the cumulative distribution of $\psi_x(t)$.

The likelihood function $\mathcal{L}$ is maximized with respect to the two parameters of the Weibull distribution (ζ, k). In the vicinity of this maximum, we approximate the likelihood by a Gaussian distribution. The estimated values for the parameter k are summarized in Table S1. All values are reasonably close to $k \approx 1$, such that an exponential run-time distribution for the modeling is justified. Note in this context that minor deviations from the exponential shape will not change the qualitative reasoning.

	flagella	direction of motion	estimate for k	2σ-confidence interval
control	push	left	0.99	$(0.85, 1.13)$
	push	right	0.94	$(0.84, 1.04)$
	wrap	left	1.03	$(0.93, 1.13)$
	wrap	right	1.00	$(0.90, 1.10)$
chemo	push	upgradient	0.79	$(0.69, 0.89)$
	push	downgradient	0.93	$(0.81, 1.05)$
	wrap	upgradient	0.91	$(0.81, 1.01)$
	wrap	downgradient	0.92	$(0.82, 1.02)$

Table S1: Parametric maximum likelihood estimates of the parameter k of the run-time distribution, modeled by a Weibull distribution [cf. Eq. (40)].

The maximum likelihood approach furthermore allows us to quantitatively compare run-time distributions in the presence of a chemical gradient. The marginal likelihood $\mathcal{L}(\zeta)$ as a function of the scale parameter ζ is graphically represented in Fig. S10; note in this context that the maximum likelihood approach is equivalent to a Bayesian approach using flat prior distributions. The analysis was performed for bacteria moving upgradient and downgradient, respectively. The analysis reveals that the relative run-time bias in the wrapped mode is much larger compared to the push mode.

From the posterior distributions of the scale parameters in up- and downgradient direction, we furthermore calculated the probability density function for the difference of these scale parameters – a vanishing difference of the scale parameters indicates the absence of a run-time bias. The obtained distributions are shown as insets in Fig. S10, where the 2σ interval is graphically highlighted as a gray shaded region. One can see that $\delta\zeta = 0$ is indeed within the 2σ-interval in the case of bacteria swimming in the push mode, whereas it lies far outside this region in the wrapped mode. To be precise, we find that the differences in the case of push swimmers correspond to a 1.6σ fluctuation, which we do not consider as statistically significant, whereas we find a 3.1σ fluctuation in the case of wrapped swimmers. It is thus reasonable to

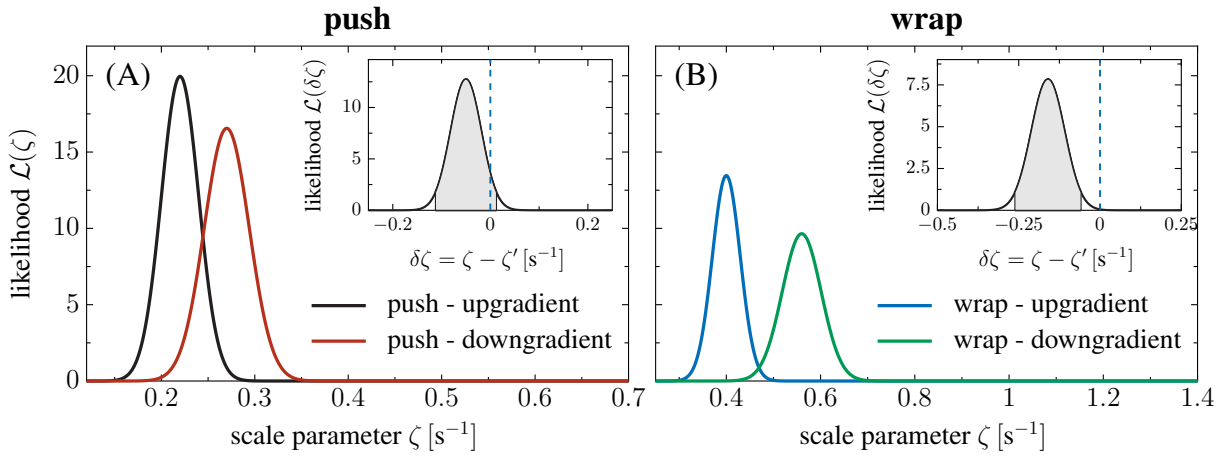

Figure S10: Inferred likelihood $\mathcal{L}$ as a function of the scale parameter ζ for swimming in the push (panel A) and wrapped mode (panel B). The insets represent the derived likelihood for the difference of scale parameters $\delta\zeta$ for up- vs. downgradient swimming; the 2σ-interval is highlighted in gray. There is a statistically significant run-time bias in the wrapped mode, whereas the difference of up- and downgradient run-time statistics in the push mode is statistically not significant.

believe that, in the case of the push swimmers, the up- and downgradient run-time distributions are indistinguishable and apparent differences are due to fluctuations, whereas in the case of wrapped swimmers, the difference between the up- and downgradient run-time distributions is statistically significant, as a 3σ-fluctuation is highly unlikely. This led us to the conclusion that the wrapped swimming mode is the dominant one for performing chemotaxis.

Applying the same analysis technique to the control data set, where no chemoattractant is present, allows us to estimate the mean run-time in push and wrapped mode, respectively. Given the maximum likelihood estimates for k and ζ, the mean run-time is calculated via

$$\langle t \rangle = \frac{\Gamma(1+1/k)}{\zeta}. \tag{43}$$

We obtained $\langle t \rangle_p = (3.3 \pm 0.3)$s for runs in the push mode and $\langle t \rangle_w = (2.3 \pm 0.2)$s in the wrapped mode, respectively. Hence, the mean transition rate used in the theoretical analysis in the main text are given by $\lambda_p \approx 0.3\,\mathrm{s}^{-1}$ and $\lambda_w \approx 0.4\,\mathrm{s}^{-1}$.

Parameters of the active particle model All model parameters that were used in the modeling part and in the theoretical discussion of the main text were estimated from experimental data; the estimates are summarized in Tab. S2 at the end of this section. In this appendix, we complement the main text by additional experimental data and provide furthermore details on the parameter estimation used to determine all model parameters of the motility pattern of *Pseudomonas putida*. However, we would like to stress that the main purpose of the modeling part is not only to reproduce the experimental observations, but simplifying assumptions are made in order to obtain a model which is both, descriptive and analytically tractable, such that the long-time dynamics of bacteria in concentration gradients can be calculated based on a physical model of the experimentally available short-time dynamics.

The analysis of the run-time statistics, which is discussed in the main text in the context of Fig. 3, was performed using the non-parametric maximum likelihood approach proposed in (*15*). It enables us to take censored data into account in an analogous way as discussed in the previous section. However, the non-parametric approach allows us to estimate the run-time statistics without implying a specific shape of the run-time distribution. Using a numerical likelihood maximization scheme, this method yields the survival time distribution

$$s(t) = \int_t^\infty du\, \psi_x(u) \tag{44}$$

and, as an additional parameter, the average run-time in the respective run-modes. The two approaches yield consistent results, i.e. the mean transition rates for the push and wrapped modes are $\lambda_p \approx 0.3\,\mathrm{s}^{-1}$ and $\lambda_w \approx 0.4\,\mathrm{s}^{-1}$, however, the error bars are larger in the non-parametric approach because there are more degrees of freedom.

The velocities of bacteria during runs were calculated using a finite difference approximation of the first derivative. The scatter plots of the obtained velocities in push and wrapped mode are represented in Fig. S11. The crater-like shape of the velocity distribution – particularly well

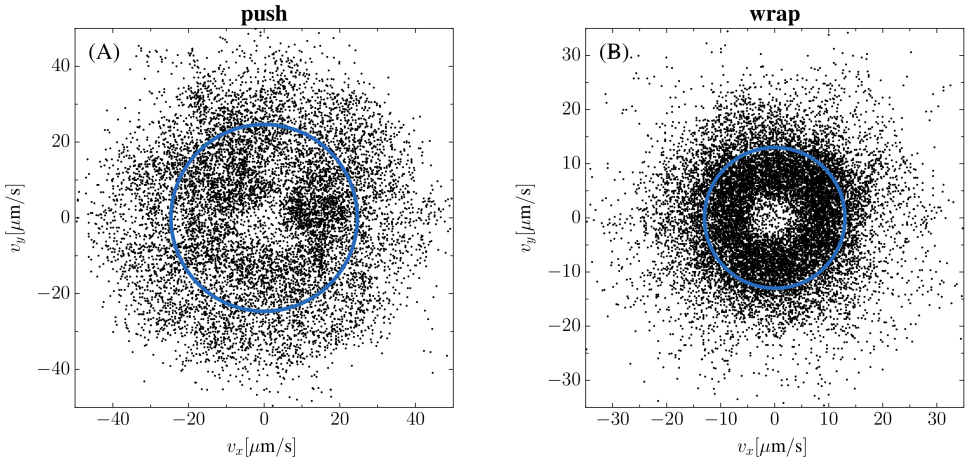

Figure S11: Scatter plots of the velocities for (A) push and (B) wrapped swimming modes from which the mean speed, shown as a blue circle, was calculated.

visible for runs in the wrapped mode – is a hallmark of self-propelled motion, as it contrasts to the Gaussian velocity distribution of passive Brownian diffusion. The ensemble average yields the speeds $v_p \approx 25\,\mu\mathrm{m/s}$ and $v_w \approx 13\,\mu\mathrm{m/s}$ for the push and wrapped modes, respectively. At this point, the model simplifies the dynamics as temporal fluctuations of the speed are not taken into account. Note, however, that the values of the speeds are of minor relevance to the discussion in the main text, as the qualitative results only depend on the speed ratio $v_p/v_w \approx 2$.

The rotational diffusion coefficients were estimated from the variances of the histograms of the angular reorientations, $\Delta\varphi(t) = \varphi(t + \Delta t) - \varphi(t)$, taken for bacteria moving at a speed comparable to the mean speed. These histograms are shown in Fig. S12 for runs in the push and wrapped mode. They are well approximated by a Gaussian density; accordingly, the angular dynamics is well-described by rotational noise. We obtained the parameter values $D_p \approx 0.03\,\mathrm{rad}^2/\mathrm{s}$ and $D_w \approx 0.13\,\mathrm{rad}^2/\mathrm{s}$, respectively. The corresponding fitted distributions are also shown in Fig. S12.

Further important parameters of the model are the average cosine of the reorientation angles for stop or reversal events: $\langle\cos\psi_{pp}\rangle$, $\langle\cos\psi_{wp}\rangle$, $\langle\cos\psi_{pw}\rangle$ and $\langle\cos\psi_{ww}\rangle$. The histograms of the

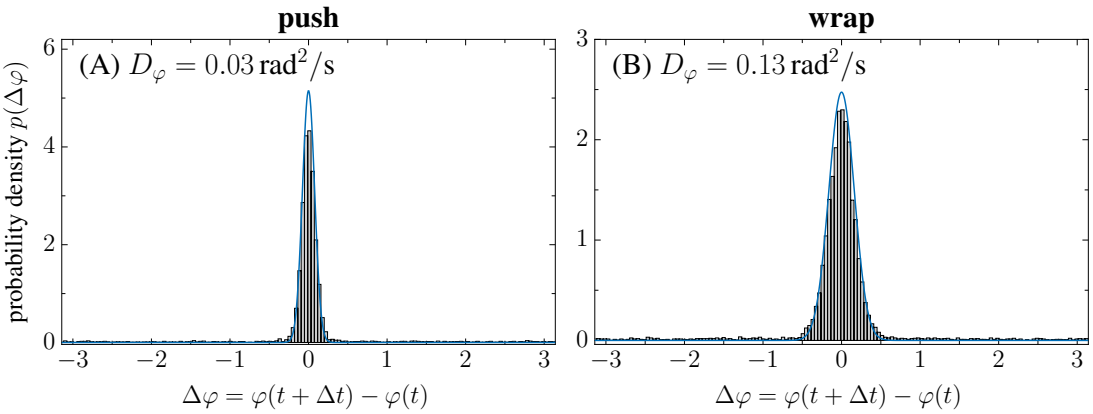

Figure S12: Histograms of the angular reorientations $\Delta\varphi(t) = \varphi(t+\Delta t) - \varphi(t)$ measured experimentally in push (panel A) and wrapped swimming mode (panel B), from which the rotational noise strengths are derived. The probability densities are well approximated by Gaussian distributions shown by blue lines, thus supporting the modeling of the angular dynamics via rotational diffusion.

observed angles are shown in the main text (Fig. 2) from which the respective averages follow immediately. Whenever a run ends, one can observe whether a run in the same swimming mode follows or, equivalently, whether the swimming mode changes and how many times each scenario occurs. By directly counting all experimentally observed transitions, we determined the estimates of the splitting probabilities to be within the 2σ confidence intervals $p_{wp} \in (0.4, 0.45)$ and $p_{pw} \in (0.7, 0.8)$.

While reversal events (push-wrap and wrap-push transitions) can be unambiguously identified based on their large turning angle, the detection of stop events is more difficult, as it depends sensitively on the choice of the parameters in the event detection scheme. It is thus crucial to verify that the model predictions are not sensitive to the identification of stop events as we will demonstrate in the following.

The way in which stop events are detected influences several quantities, in particular, the transition probabilities p_{wp} and p_{pw} and the run-time distributions in up- and downgradient direction. If the number of stop events is overestimated, the run-times decrease but the probability

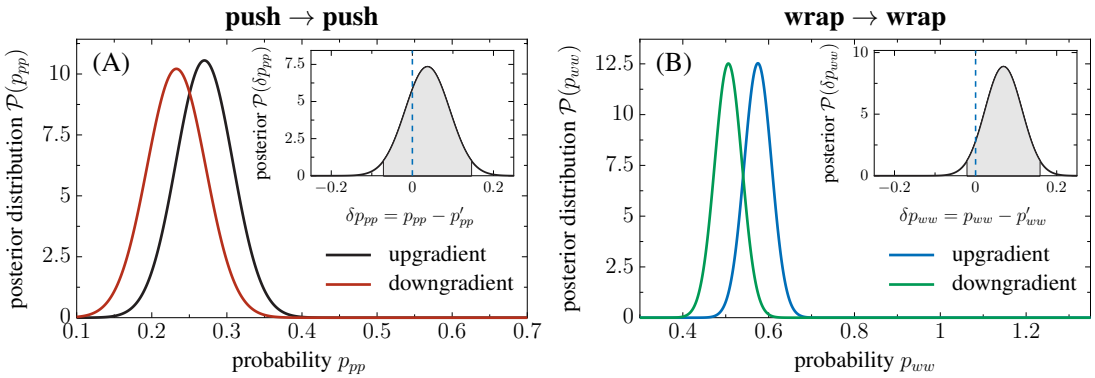

Figure S13: Posterior probability density for the model parameters p_{pp} (panel A) and p_{ww} (panel B), distinguished according to the direction of motion of bacteria with respect to the chemical gradient. The insets show the probability density functions for the up-down-gradient difference of these parameters, where additionally the 2σ interval is highlighted in gray. We find that the difference in the case of push-push transitions (panel A) – equivalently push-wrap transitions – corresponds to a 0.7σ fluctuation and, in the case of wrap-wrap transitions (panel B), to a 1.5σ fluctuation. Accordingly, the apparent difference of the parameter values up- and downgradient is statistically insignificant, i.e. the probabilities p_{pp}, p_{ww}, p_{pw} and p_{wp} are constant parameters, independent of the direction of motion.

that a push (wrapped) run is followed by another push (wrapped) run in the same direction increases, resulting in the same net displacement in a given direction. We thus expect that the overall chemotactic drift coefficient μ is robust with respect to moderate errors in the detection scheme of stop events.

From the modeling perspective, it is crucial that we assume that the mean run-times depend on the chemical gradient (the durations of runs in up- and down-gradient direction differ), while the transition probabilities p_{wp} and p_{pw} are constant parameters (independent of the direction of motion with respect to the chemical gradient). If the number of stops was overestimated, the parameters $p_{wp} = (1 - p_{ww})$ and $p_{pw} = (1 - p_{pp})$ would become dependent on the direction of motion with respect to the chemical gradient as well. In this case, upgradient runs in wrapped mode, in contrast to downgradient wrapped runs, would be more likely to be followed by another wrapped run in the same direction. Using Bayesian inference, we convinced ourselves that

these probabilities, inferred from our event detection algorithm, are indeed independent of the gradient direction. The likelihood for the counting experiment is determined by the binomial distribution

$$P(k|N,p) = \binom{N}{k} p^k (1-p)^{N-k} \tag{45}$$

such that, using a flat prior, the posterior distribution is given by a beta distribution

$$f(p|\alpha,\beta) = \frac{\Gamma(\alpha+\beta)}{\Gamma(\alpha)\,\Gamma(\beta)}\, p^{\alpha-1}(1-p)^{\beta-1} \tag{46}$$

with $\alpha = k{+}1$ and $\beta = N{-}k{+}1$, where N is the total number of transitions and k is the number of transitions along a certain channel, i.e. from push (wrap) to push (wrap). The posterior distributions are displayed in Fig. S13, where we show both, the inferred distributions as well as the probability density functions of the differences of the respective probabilities (insets of Figs. S13) for the push-push and wrap-wrap transitions. We find that the difference in the case of push-push transitions (equivalently push-wrap transitions) corresponds to a 0.7σ fluctuation and, in the case of wrap-wrap transitions, to a 1.5σ fluctuation, which in both cases we do not consider as statistically significant. Therefore, we do believe that our way of estimating stop events is meaningful.

model parameter	**estimated mean value**
D_p	$0.03\,\mathrm{s}^{-1}$
D_w	$0.13\,\mathrm{s}^{-1}$
v_p	$25\,\mu\mathrm{m/s}$
v_w	$13\,\mu\mathrm{m/s}$
λ_p	$0.3\,\mathrm{s}^{-1}$
λ_w	$0.4\,\mathrm{s}^{-1}$
p_{wp}	0.42
p_{pw}	0.75
$\langle\cos\psi_{pp}\rangle$	0.9
$\langle\cos\psi_{pw}\rangle$	-0.9
$\langle\cos\psi_{wp}\rangle$	-0.9
$\langle\cos\psi_{ww}\rangle$	0.55

Table S2: The table summarizes the mean values of model parameters as they were estimated from experimental data.

REFERENCES AND NOTES

1. H. C. Berg, *E. coli in Motion* (Springer, 2004).

2. H. C. Berg, D. A. Brown, Chemotaxis in *Escherichia coli* analysed by three-dimensional tracking. *Nature* **239**, 500–504 (1972).

3. J. P. Armitage, R. M. Macnab, Unidirectional, intermittent rotation of the flagellum of Rhodobacter sphaeroides. *J. Bacteriol.* **169**, 514–518 (1987).

4. J. E. Johansen, J. Pinhassi, N. Blackburn, U. L. Zweifel, Å. Hagström, Variability in motility characteristics among marine bacteria. *Aquat. Microb. Ecol.* **28**, 229–237 (2002).

5. T. Mukherjee, M. Elmas, L. Vo, V. Alexiades, T. Hong, G. Alexandre, Multiple CheY homologs control swimming reversals and transient pauses in *Azospirillum* brasilense. *Biophys. J.* **116**, 1527–1537 (2019).

6. J.-B. Raina, V. Fernandez, B. Lambert, R. Stocker, J. R. Seymour, The role of microbial motility and chemotaxis in symbiosis. *Nat. Rev. Microbiol.* **17**, 284–294 (2019).

7. M. Hintsche, V. Waljor, R. Großmann, M. J. Kühn, K. M. Thormann, F. Peruani, C. Beta, A polar bundle of flagella can drive bacterial swimming by pushing, pulling, or coiling around the cell body. *Sci. Rep.* **7**, 16771 (2017).

8. K. J. Duffy, R. M. Ford, Turn angle and run time distributions characterize swimming behavior for Pseudomonas putida. *J. Bacteriol.* **179**, 1428–1430 (1997).

9. M. Theves, J. Taktikos, V. Zaburdaev, H. Stark, C. Beta, A bacterial swimmer with two alternating speeds of propagation. *Biophys. J.* **105**, 1915–1924 (2013).

10. M. J. Kühn, F. K. Schmidt, B. Eckhardt, K. M. Thormann, Bacteria exploit a polymorphic instability of the flagellar filament to escape from traps. *Proc. Natl. Acad. Sci. U.S.A.* **114**, 6340–6345 (2017).

11. M. A. Constantino, M. Jabbarzadeh, H. C. Fu, Z. Shen, J. G. Fox, F. Haesebrouck, S. K. Linden, R. Bansil, Bipolar lophotrichous *Helicobacter suis* combine extended and wrapped flagella bundles to exhibit multiple modes of motility. *Sci. Rep.* **8**, 14415 (2018).

12. Y. Kinosita, Y. Kikuchi, N. Mikami, D. Nakane, T. Nishizaka, Unforeseen swimming and gliding mode of an insect gut symbiont, *Burkholderia* sp. RPE64, with wrapping of the flagella around its cell body. *ISME J.* **12**, 838–848 (2018).

13. L. Turner, L. Ping, M. Neubauer, H. C. Berg, Visualizing flagella while tracking bacteria. *Biophys. J.* **111**, 630–639 (2016).

14. L. Xie, T. Altindal, S. Chattopadhyay, X.-L. Wu, Bacterial flagellum as a propeller and as a rudder for efficient chemotaxis. *Proc. Natl. Acad. Sci. U.S.A.* **108**, 2246–2251 (2011).

15. Y. Vardi, Nonparametric estimation in renewal processes. *Ann. Statist.* **10**, 772–785 (1982).

16. T. Altindal, L. Xie, X.-L. Wu, Implications of three-step swimming patterns in bacterial chemotaxis. *Biophys. J.* **100**, 32–41 (2011).

17. L. Xie, C. Lu, X.-L. Wu, Marine bacterial chemoresponse to a stepwise chemoattractant stimulus. *Biophys. J.* **108**, 766–774 (2015).

18. M. J. Schnitzer, Theory of continuum random walks and application to chemotaxis. *Phys. Rev. E* **48**, 2553–2568 (1993).

19. O. Pohl, M. Hintsche, Z. Alirezaeizanjani, M. Seyrich, C. Beta, H. Stark, Inferring the chemotactic strategy of *P. putida* and *E. coli* using modified Kramers-Moyal coefficients. *PLOS Comput. Biol.* **13**, e1005329 (2017).

20. P.-G. De Gennes, Chemotaxis: The role of internal delays. *Eur. Biophys. J.* **33**, 691–693 (2004).

21. J. T. Locsei, Persistence of direction increases the drift velocity of run and tumble chemotaxis. *J. Math. Biol.* **55**, 41–60 (2007).

22. A. Celani, M. Vergassola, Bacterial strategies for chemotaxis response. *Proc. Natl. Acad. Sci. U.S.A.* **107**, 1391–1396 (2010).

23. J. Taktikos, H. Stark, V. Zaburdaev, Correction: How the motility pattern of bacteria affects their dispersal and chemotaxis. *PLOS ONE* **8**, e81936 (2013).

24. M. Seyrich, A. Palugniok, H. Stark, Traveling concentration pulses of bacteria in a generalized Keller–Segel model. *New J. Phys.* **21**, 103001 (2019).

25. L. G. Nava, R. Großmann, F. Peruani, Markovian robots: Minimal navigation strategies for active particles. *Phys. Rev. E* **97**, 042604 (2018).

26. E. F. Keller, L. A. Segel, Model for chemotaxis. *J. Theor. Biol.* **30**, 225–234 (1971).

27. F. Thiel, L. Schimansky-Geier, I. M. Sokolov, Anomalous diffusion in run-and-tumble motion. *Phys. Rev. E* **86**, 021117 (2012).

28. E. M. Lifshitz, L. P. Pitaevskii, *Physical Kinetics, vol. 10 of Course of Theoretical Physics* (Pergamon Press, 1981).

29. D. López-Farfán, J. A. Reyes-Darias, M. A. Matilla-Vazquez, T. Krell, Concentration dependent effect of plant root exudates on the chemosensory systems of *Pseudomonas putida* KT2440. *Front. Microbiol.* **10**, 78 (2019).

30. K. Son, J. S. Guasto, R. Stocker, Bacteria can exploit a flagellar buckling instability to change direction. *Nat. Phys.* **9**, 494–498 (2013).

31. E. Belda, R. G. A. van Heck, M. José Lopez-Sanchez, S. Cruveiller, V. Barbe, C. Fraser, H.-P. Klenk, J. Petersen, A. Morgat, P. I. Nikel, D. Vallenet, Z. Rouy, A. Sekowska, V. A. P. Martins dos Santos, V. de Lorenzo, A. Danchin, C. Médigue, The revisited genome of *Pseudomonas putida* KT2440 enlightens its value as a robust metabolicchassis. *Environ. Microbiol.* **18**, 3403–3424 (2016).

32. J.-B. Masson, G. Voisinne, J. Wong-Ng, A. Celani, M. Vergassola, Noninvasive inference of the molecular chemotactic response using bacterial trajectories. *Proc. Natl. Acad. Sci. U.S.A.* **109**, 1802–1807 (2012).

33. A. Savitzky, M. J. E. Golay, Smoothing and differentiation of data by simplified least squares procedures. *Anal. Chem.* **36**, 1627–1639 (1964).

34. B. Efron, R. J. Tibshirani, *An introduction to the bootstrap* (Chapman and Hall/CRC, 1994).

35. P. Zengel, A. Nguyen-Hoang, C. Schildhammer, R. Zantl, V. Kahl, E. Horn, μ-Slide Chemotaxis: A new chamber for long-term chemotaxis studies. *BMC Cell Biol.* **12**, 21 (2011).

36. J. N. Kapur, P. K. Sahoo, A. K. C. Wong, A new method for gray-level picture thresholding using the entropy of the histogram. *Comput. Vis. Graph.* **29**, 273–285 (1985).

37. J. C. Crocker, D. G. Grier, Methods of digital video microscopy for colloidal studies. *J. Coll. Interfat. Sci.* **179**, 298–310 (1996).

38. R. Großmann, F. Peruani, M. Bär, A geometric approach to self-propelled motion in isotropic & anisotropic environments. *Eur. Phys. J. Spec. Top.* **224**, 1377–1394 (2015).

39. C. Godrèche, J. M. Luck, Statistics of the occupation time of renewal processes. *J. Stat. Phys.* **104**, 489–524 (2001).